CHEMISTRY OF MATERIALS

pubs.acs.org/cm

Article

Size-Controlled Templating of Stable Drug Nanoparticles from Nanoemulsion Precursors for Versatile Nanoformulation

Lucas Attia,[†] Dien Nguyen,[†] Kevin Liu, Qin M. Qi, and Patrick S. Doyle*

Cite This: https://doi.org/10.1021/acs.chemmater.5c02892

Read Online

ACCESS | Metrics & More | Article Recommendations | Supporting Information

ABSTRACT: Nanosizing drug particles has emerged as a successful approach to enable the oral bioavailability of lipophilic small molecule drugs. Scalable "bottom-up" methods have been developed to overcome the limitations and resource-intensiveness of traditional "top-down" nanoparticle production. However, bottom-up approaches are still limited in their applicability across drug chemistries, their ability to control particle size distributions, and the long-term stability of the generated nanoparticles. Here, we overcome these limitations by applying a versatile nanoemulsion templating approach to generate drug nanoparticle formulations inside a hydrogel thin film. By using different dispersed phase solvents, we formulate four chemically diverse drug molecules. Nanoparticle size is precisely tuned by controlling precursor nanoemulsion droplet size, enabling customizable formulations between 100−1000 nm. The resulting nanoparticles retain stable size distributions and solid states for at least six months at room temperature. We demonstrate the *in vitro* bioavailability enhancement of our nanoformulations through dramatically faster dissolution, increased apparent thermodynamic solubility, and enhanced permeability across Caco-2 cell monolayers. Notably, we quantitatively measure the solubility enhancement as a function of nanoparticle size and report a rare validation of the Ostwald−Freundlich equation. The thin-film form factor of our nanoformulations could enable applications in buccal delivery, oral delivery for pediatric, elderly, or dysphagic patients, and "suspensions-on-demand" for stable storage of point-of-care nanoparticle suspensions. Together, this work introduces a general, tunable, and shelf-stable platform for rapid fit-for-purpose pharmaceutical nanoformulations.

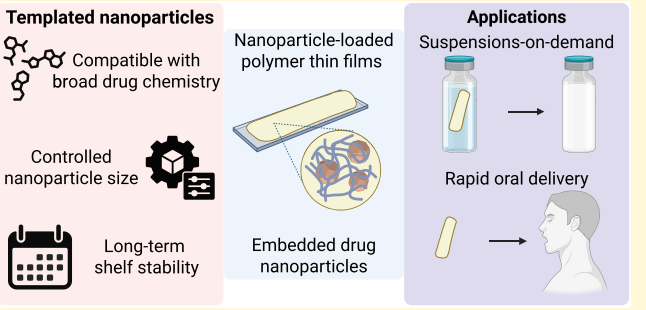

1. INTRODUCTION

The lipophilicity of most small molecules drug candidates limits their clinical bioavailability and remains a major cause of clinical trial failures. Researchers estimate that 15−50% of clinical trial failures are a result of poor oral bioavailability; these expensive failures contribute to increasing drug product costs.[1−3] Lipophilic molecules exhibit low aqueous solubility, slow dissolution, and even comparatively higher toxicity due to promiscuity.[2,4,5] Since nearly 90% of drug candidates are lipophilic, there has been substantial interest in developing enabling formulation approaches that can overcome these limitations. As emerging drug candidates trend toward larger molecular weights[6] and increasingly complex molecules like PROTACs,[7] the need to overcome lipophilicity through engineered formulations is becoming more urgent.

Reducing drug aggregate size to the nanoscale has been an effective strategy to enable the oral formulation of lipophilic active pharmaceutical ingredients (APIs), since nanoparticles ($d_{\text{nanoparticle}}$ < 1000 nm) exhibit higher apparent solubility and faster dissolution kinetics.[4,8] Traditionally, such nanoformulations have been manufactured "top-down", wherein large drug crystals are mechanically milled down to the nanoscale.[9] However, top-down manufacturing is time- and energy-intensive, risks contamination from milling media, can induce polymorphic changes, and offers limited control over the particle size distribution (PSD).[9−11] In response, "bottom-up" methods have been developed to overcome some of these challenges by directly assembling nanosized drug aggregates through precipitation or evaporation.[12] Bottom-up approaches, including flash nanoprecipitation (FNP),[13,14] evaporative precipitation into aqueous solution (EPAS),[15] supercritical fluid processing,[16,17] and emulsion templating[18] can leverage the benefits of excipients during solidification to control drug particulate morphology.[19] However, these technologies have limited generality. Specifically, controlling the PSD is a challenge with EPAS[20] and traditional emulsion templating.[18] In supercritical fluid processes, it is challenging to form nanoparticles for lipophilic APIs and to decouple API

Received: October 28, 2025
Revised: December 18, 2025
Accepted: December 19, 2025

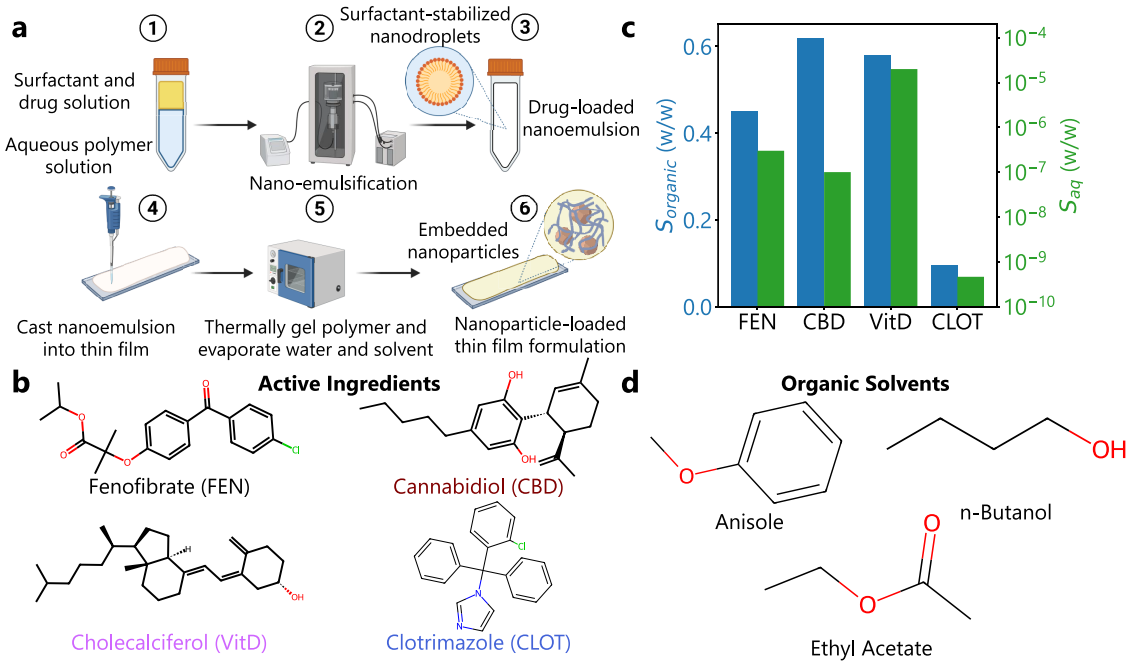

Figure 1. Nanosizing structurally diverse lipophilic active ingredients using nanoemulsion templating. (a) Overview of nanoemulsion templating process inside hydrogel thin films. The active ingredient is dissolved in an organic solvent. This solution is nanoemulsified in a polymer solution using ultrasonication and (optionally) surfactant. The nanoemulsion is cast into a thin film, and dried to template size-controlled drug nanoparticles embedded and stabilized in a polymer matrix. (b) Molecular structures of the active ingredients used in this study. The abbreviations for the active ingredients shown in parentheses are referenced throughout this work. (c) Water solubility, S_{aq} (right, green), and organic solvent concentration, $S_{organic}$ (left, blue) of active ingredients used in this study, determined as discussed in Supporting Information Section S1. Both the water solubility in solvent concentration are in weight fraction. Fenofibrate (FEN) and cannabidiol (CBD) are dissolved in anisole; cholecalciferol (VitD) is dissolved in ethyl acetate; clotrimazole (CLOT) is dissolved in *n*-butanol. (d) Molecular structures of the organic solvents used in this study.

lipophilicity from particle size.[16,21] While FNP can generate size-controlled suspensions,[22] drug stability is limited by drug concentration[23] and lipophilicity,[24] and PSDs typically remain stable for only a few days. Our research group has developed a nanoemulsion templating approach where drug nanoparticles are simultaneously templated and formulated inside hydrogel matrices from nanoemulsion precursors.[25−27] This approach enables the generation of monodisperse nanoparticles,[28] controlled drug release through hydrogel design,[29,30] and adaptation to versatile formulation form factors.[25,31] However, we have not demonstrated applicability to diverse API chemistry, precise control over nanoparticle size, or long-term PSD stability.

Here, we overcome these challenges by demonstrating a versatile nanoemulsion templating approach within polymeric thin films to produce size-controlled nanoparticles. We validate our approach across four diverse API classes: fibrates, cannabinoids, steroids, and azoles. We highlight precise nanoparticle size control over a wide size range (100−900 nm) and PSD shelf-stability over several months through storage in the polymeric thin film. The templated nanoparticles are readily resuspendable from the thin film matrix, providing a route to stable nanoparticle suspensions. Finally, we demonstrate significant kinetic dissolution and Caco-2 permeability enhancement of our nanoformulations and provide a rare quantitative validation of the Ostwald−Freundlich relationship between solubility and nanoparticle size. Overall, this work expands the generalizability of nanoemulsion templating and unlocks the efficient formulation of lipophilic APIs using this technology.

2. RESULTS AND DISCUSSION

2.1. Design of Nanoemulsions Loaded with Chemically Diverse Lipophilic Actives

As previously mentioned, we apply nanoemulsion templating in a simple hydrogel thin film form factor (Figure 1a). In this scheme, the nanoemulsion is designed with thermogelling capability through a thermogelling polymer in the continuous phase. We use methylcellulose (MC), an FDA-approved excipient with a generally recognized as safe (GRAS) designation,[32] which gels thermally near body temperature.[25] In these nanoemulsions, the dispersed organic phase contains only the API-loaded solvent, the continuous phase consists of 5 wt % MC aqueous solution, and surfactant, which is included to control emulsification and stabilize droplets (see Supporting Information Section S1 for formulation details). We used either polysorbate 80 (Tween80) or sorbitan monooleate 80 (Span80), both GRAS excipients, as the surfactant. After generating the drug-loaded nanoemulsion, it is cast onto a glass substrate, then gelled and dried in an oven. While this study focuses on nanoemulsion design, size-control, and stability across broad API chemistry, the thin film form factor is highly relevant to several oral drug delivery applications. Specifically, thin films are crucial to deliver therapeutics to patient populations who cannot swallow pills, including pediatric, geriatric, psychiatric, and dysphagic patients.[33] Additionally, thin films are advantageous for rapid release in emergent conditions,[34] including anaphylaxis and seizure.

We selected four chemically diverse lipophilic APIs to demonstrate the versatility of our approach (Figure 1b). Fenofibrate (FEN) is a model lipophilic drug with extremely low water solubility (S_{aq} = 3 × 10^{-7} w/w, log *P* = 4.86), which

https://doi.org/10.1021/acs.chemmater.5c02892
Chem. Mater. XXXX, XXX, XXX−XXX

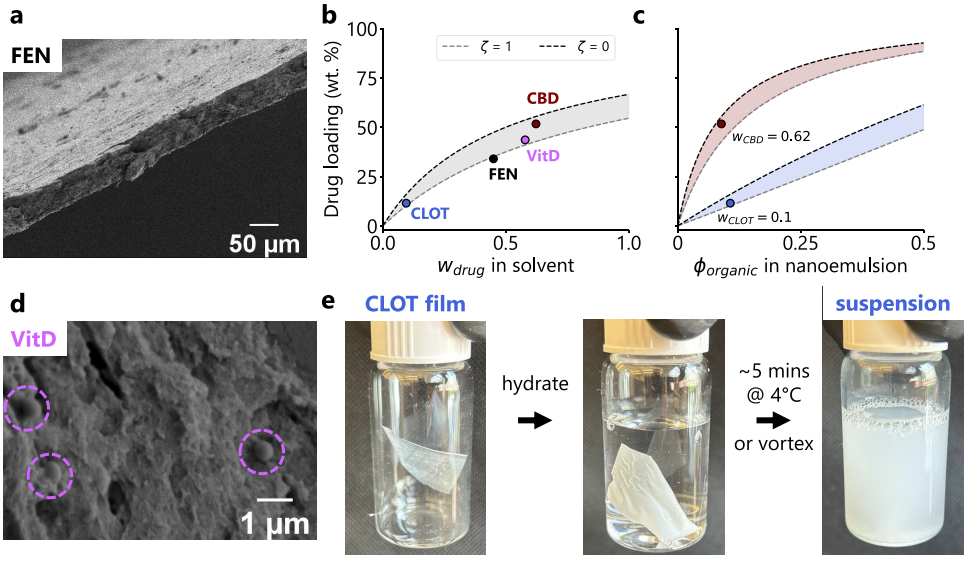

Figure 2. Nanoparticle-loaded thin polymer films. (a) SEM micrograph showing the cross-section of a thin film loaded with FEN nanoparticles. Scale bar represents 50 μm. (b, c) Drug loading in wt % in the dried thin films as a function of (b) the wt. fraction of drug in the organic solvent (w_{drug}) and (c) the volume fraction of organic solvent in the nanoemulsion ($\phi_{solvent}$). Solid points represent measured drug loading. Black dashed line represents $\zeta = 0$ (no surfactant is retained after drying), while gray dashed line represents $\zeta = 1$ (all surfactant is retained after drying). (d) SEM micrograph showing VitD nanoparticles embedded in thin film. Nanoparticles are circled in dotted lines. Scale bar represents 1 μm. (e) Digital images demonstrating how to extract embedded nanoparticles from the thin films. A vial containing a CLOT film is filled with water, then either refrigerated at 4 °C for 5 min or vortexed for 1 min to dissolve the MC film and release nanoparticles, forming a CLOT nanosuspension.

has been widely used in nanoformulation research[35] and is commercially available as a nanoformulation, TriCor. Cannabidiol (CBD, $S_{aq} = 1 \times 10^{-7}$ w/w, $\log P = 6.1$),[36] cholecalciferol (VitD, $S_{aq} = 2 \times 10^{-5}$ w/w, $\log P = 7.98$)[37] and clotrimazole (CLOT, $S_{aq} = 4.6 \times 10^{-10}$ w/w, $\log P = 5.48$)[38] have also generated substantial interest in nanoformulation due to their low aqueous solubility and poor bioavailability (Figure 1c). These APIs are representative of their lipophilic drug classes which suffer from low bioavailability: fibrates, cannabinoids, steroids, and azoles. By applying nanoemulsion templating to this representative subset of lipophilic APIs, this work provides design guidelines for how this process would be adapted to an untested API candidate.

The first design consideration is the solubility of the API in a suitable organic solvent. Suitable organic solvents must have limited or no water miscibility and must evaporate at accessible temperature and pressure conditions. We also constrain the solvent selection to FDA class 3 solvents, which have low or no toxic potential.[39] Since the API organic solubility has implications in the drug loading of the film, we select solvents that give a range of API solubility. FEN ($S_{organic} = 0.45$ w/w)[28] and CBD ($S_{organic} = 0.62$ w/w) are dissolved in anisole, VitD ($S_{organic} = 0.58$ w/w) is dissolved in ethyl acetate, and CLOT ($S_{organic} = 0.095$ w/w)is dissolved in *n*-butanol (Figure 1c,d). The solubility determination for CBD, VitD, and CLOT in anisole, ethyl acetate, and *n*-butanol respectively are detailed in Supporting Information Section S2.

The resulting thin films are qualitatively observed to be mechanically pliable and robust to bending (Supporting Information Figure S4).[31] Scanning electron microscopy (SEM) reveals the uniform cross section of a FEN-loaded thin film, which has a thickness of 52 μm (Figure 2a). The film thickness can be controlled by the amount of nanoemulsion cast onto the substrate. The API loading in the thin film can be tuned through multiple parameters, including the API concentration in the organic phase (w_{drug}) and the volume fraction of the organic solvent in the nanoemulsion ($\phi_{solvent}$). First, w_{drug} can be varied up to the solubility limit ($S_{organic}$), which in turn sets the API loading in the film according to eq 1 below.

$$\text{drug loading \%} = \frac{w_{drug} m_{solvent}}{w_{drug} m_{solvent} + w_{MC} m_{aq} + \zeta_{surf} m_{surf}} \cdot 100 \quad (1)$$

where $m_{solvent}$ is the mass (g) of the organic phase in the nanoemulsion, w_{MC} is the weight fraction of MC in the aqueous phase (0.05), m_{aq} is the mass of the aqueous phase (g), ζ_{surf} is the retention fraction of the surfactant in the film after drying, and m_{surf} is the mass of surfactant (g) in the nanoemulsion. The surfactant retention ζ_{surf} accounts for the partial evaporation of surfactant from the formulation during drying. The effect of w_{drug} on drug loading in the film is demonstrated by comparing the drug loading between films containing different APIs, keeping all other formulation components constant (Figure 2b). Drug loading is highest for CBD (51.7%) and lowest for CLOT (11.5%). Additionally, $\phi_{organic}$, defined below in eq 2, also directly controls the drug loading, since the API is dissolved in the organic solvent

$$\phi_{organic} = \frac{V_{organic}}{V_{organic} + V_{aq} + V_{surfactant}} \quad (2)$$

where $V_{organic}$ is the dispersed phase volume, V_{aq} is the continuous aqueous phase volume, and $V_{surfactant}$ is the volume of surfactant in the nanoemulsion. The dependence of drug loading on $\phi_{organic}$ is demonstrated in Figure 2c. For CBD, which has the highest organic solubility ($w_{drug} = 0.62$), drug loading first sharply increases as $\phi_{organic}$drug loading increases, then plateaus for higher dispersed phase volume fractions. For CLOT, which has the lowest organic solubility ($w_{drug} = 0.095$), drug loading responds nearly linearly with increasing $\phi_{organic}$, since w_{drug} is much lower. The analytical determination of drug

https://doi.org/10.1021/acs.chemmater.5c02892
Chem. Mater. XXXX, XXX, XXX−XXX

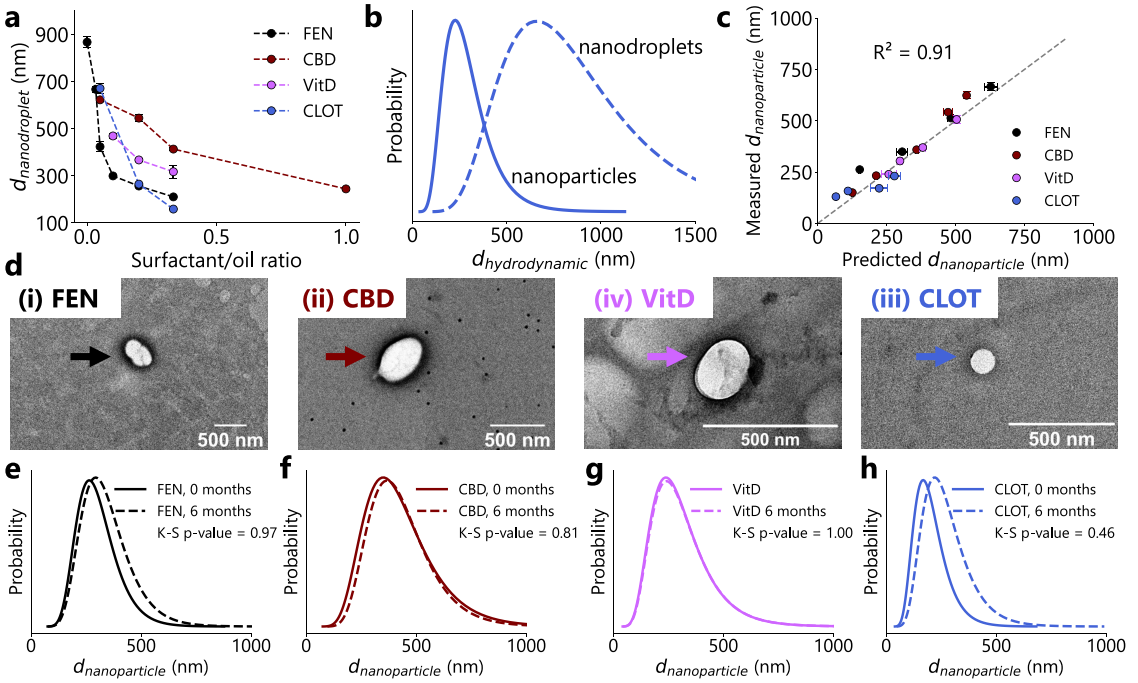

Figure 3. Size-controlled drug nanoparticles are templated from drug-loaded nanodroplets. (a) Mean nanodroplet diameter $d_{\text{nanodroplet}}$ as measured using DLS as a function of the surfactant:oil ratio (SOR). The series show droplets of different drug-loaded solvents. *Y*-axis error bars represent the standard deviation in 5 DLS measurements of $d_{\text{nanodroplet}}$. (b) DLS distributions of CLOT-loaded nanodroplets (dashed line) and corresponding templated CLOT nanoparticles (solid line), demonstrating the scaling relationship in eq 3. This formulation was emulsified using Span80 as the surfactant at an SOR of 1:20 (Supporting Information Table S1). (c) Parity plot of measured mean drug nanoparticle diameter ($d_{\text{nanoparticle}}$) against theoretical $d_{\text{nanoparticle}}$ predicted from eq 3. (d) Representative TEM images of liberated nanoparticles of (i) FEN, (ii) CBD, (iii) VitD, and (iv) CLOT formulated with SOR 1:3, indicated by arrows. Scale bar represents 500 nm. Additional TEM images of liberated nanoparticles provided in Supporting Information Section S6. (e–h) DLS traces demonstrating stability of nanoparticle size distributions for (e) FEN, (f) CBD, (g) VitD, and (h) CLOT nanoformulations after 6 months of shelf storage. The Kolmogorov–Smirnov test is used to compare the DLS distributions at 0 months (solid line) and 6 months (dashed line) for each API, with the resulting *p*-values provided on each plot.

loading is provided in Supporting Information Section S4. By examining the microstructure of a VitD-loaded film under SEM, we can easily observe embedded VitD nanoparticles throughout the MC polymer matrix (Figure 2d). SEM micrographs highlighting embedded nanoparticles of the other APIs are provided in Supporting Information Section S3. These API nanoparticles can be readily liberated from the MC thin film through refrigeration or vortex mixing (Figure 2e). To demonstrate this, a CLOT nanoparticle-loaded thin film was added into a vial, then submerged in 15 mL of water, which rehydrates the MC network. MC gelation is thermoreversible, and refrigeration for a few minutes reverses the film to the sol state, liberating the embedded nanoparticles and resulting in a nanosuspension. Alternatively, the thin film can be vortexed for about 1 min to redisperse the nanoparticles.

We produce nanoformulations for APIs with diverse drug chemistry, highlighting the versatility of our approach. These APIs cover a range of log *P* (4.86–7.98) which is generally challenging for other approaches. For example, FNP nanoparticles show fast Ostwald ripening and interparticle recrystallization when $2 < \log P < 9$.[24] Recently, a variation of FNP, Sequential NanoPrecipitation (SNaP), has been shown to produce nanoparticles of APIs with lower log*P* values, albeit with relatively low encapsulation efficiencies (<50%).[40,41] Supercritical fluid processes for nanoparticle generation are sensitive to the API solubility in CO_2, which limits applicability to very lipophilic APIs.[16] Our approach is suitable for a broad range of lipophilic APIs. To apply our approach to an untested API candidate, the rate limiting step is selecting a suitable organic solvent in which the API has sufficient solubility. However, solvent selection can be accelerated through virtual screening, for example using our machine learning model FASTSOLV.[42]

Thin film formulations are often limited by low drug loadings.[34,43] In contrast, our thin film nanoformulations achieve *de facto* high drug loadings without optimization, due to the high organic phase solubility of lipophilic APIs. Our approach exhibits tunable drug loading through simple formulation parameters, w_{drug} and ϕ_{organic}. Traditional nanocarriers like nanoemulsions, micelles, and liposomes achieve drug loadings <20 wt % with poor tunability.[24] In nanoprecipitation, drug loading depends partly on drug–polymer interactions, limiting precise control. FNP formulations typically achieve 30–50 wt % drug loading,[24,44] though recent adaptations have reached higher loadings at the expense of nanoparticle size control.[45] We also estimated the residual solvent level in the dried polymer films using thermogravimetric analysis (TGA). For a FEN-loaded film, we estimated that (conservatively) 0.8% of the dried films is residual anisole by mass, suggesting our films could be used directly as dosage forms without further modification for most APIs (Supporting Information Section S13). Additionally, the ease of redispersing embedded nanoparticles to form nanosuspensions from the thin-film formulations highlights their potential as a practical storage medium for nanoformulations. The thin films already contain stabilizing excipients which we hypothesized could confer long-term nanoparticle stability, which has long been a

https://doi.org/10.1021/acs.chemmater.5c02892
Chem. Mater. XXXX, XXX, XXX–XXX

challenge in nanoformulation. The application of our nanoparticle thin films as 'suspensions-on-demand' is further established through our long-term stability characterization, summarized below.

2.2. Nanoemulsion Droplet Size Distribution Controls Drug Nanoparticle Size Distribution

After establishing that we could apply nanoemulsion templating to this diverse set of APIs in a thin film form factor, we sought to rigorously control the nanodroplet and nanoparticle size distributions. The *in vivo* fate of API nanoparticles is sensitive to their PSD, which influences biodistribution, dissolution rate, clearance, immune cell uptake, membrane permeability, and mucosal interactions.[4,46,47] Several formulation and processing parameters can control nanodroplet size, including the surfactant:oil ratio (SOR), hydrophilic lipophilic balance (HLB) of the surfactant, viscosity ratio between the dispersed and continuous phases, and power input into the emulsification.[48] Here, we demonstrate that the SOR offers facile control over the droplet size over a wide dynamic range. We varied the SOR for each API until we covered droplet sizes ranging between 100 and 900 nm. Figure 3a shows the average nanodroplet diameter ($d_{\text{nanodroplet}}$) measured via dynamic light scattering (DLS) as a function of SOR for each drug. The droplet size distributions from DLS for each of these formulations are provided in Supporting Information Figure S6, and the average $d_{\text{nanoparticle}}$ and polydispersity index (PDI) are provided in Supporting Information Table S3.

Critically, this control over nanodroplet size confers control over the templated nanoparticle size. Applying mass conservation on the drug in a single droplet and its templated particle, and describing both with an equivalent spherical average diameter, results in the relationship below in eq 3

$$d_{\text{nanoparticle}} = d_{\text{droplet}}\left(\frac{w_{\text{drug}}\rho_{\text{droplet}}}{\rho_{\text{nanoparticle}}}\right)^{1/3} \tag{3}$$

where $d_{\text{nanoparticle}}$ is the diameter of the templated nanoparticle (nm), d_{droplet} is the diameter of the droplet (nm), ρ_{droplet} is the density of the drug-loaded organic solution (kg m^{-3}), and $\rho_{\text{nanoparticle}}$ is the density of the templated nanoparticle (kg m^{-3}). This scaling between the droplet size and particle size is demonstrated qualitatively in Figure 3b, which shows how the measured size distribution CLOT-loaded droplets ($d_{\text{nanodroplet}}$ = 670.9 nm, dotted curve) shifts after solvent evaporation to form the CLOT nanoparticles ($d_{\text{nanoparticle}}$ = 230.5 nm, solid curve). To demonstrate robust size control over the templated API nanoparticles, eq 3 was used to predict the mean $d_{\text{nanoparticle}}$ using the measured $d_{\text{nanodroplet}}$. These predictions were validated by redispersing the API-loaded thin films in water, liberating the nanoparticles from the polymer matrix, then measuring the size distributions using DLS. Across 17 formulations of the four APIs, we observe excellent agreement between the predicted and measured $d_{\text{nanoparticle}}$, with R^2 = 0.91 (Figure 3c). The liberated nanoparticles were also visualized using transmission electron microscopy (TEM), where several individual nanoparticles were imaged (Figure 3d). We observe that the liberated nanoparticles are spheroidal, agreeing with the results of SEM imaging of the embedded nanoparticles (Figure 2d). Additionally, TEM imaging of liberated nanoparticles supports the DLS measurements from Figure 3c (Supporting Information Section S6).

To further establish the application of the thin film nanoformulations as a storage media for nanosuspensions, we characterized the solid form and colloidal stability of the nanoformulations after 6 months of storage at room temperature and pressure. First, we measured the colloidal stability of the nanoparticle size distributions. Excitingly, the nanoparticle size distributions stay consistent over at least 6 months (Figure 3e–h). We used a Kolmogorov–Smirnov test to compare the DLS size distributions at 0 and 6 months of storage, and found no statistically significant differences. We also characterized the stability of the solid form of the API nanoparticles using X-ray diffraction (XRD) and differential scanning calorimetry (DSC), finding that the nanoparticle solid form also remained stable. Consistent with our group's previous work,[25,31,49] we found that templated FEN nanoparticles were crystalline and were stable for at least 6 months after storage. However, we found that CBD, CLOT, and VitD nanoparticles were amorphous and similarly exhibited stability for at least 6 months, with no detectable crystalline signal appearing in our characterization. See Supporting Information Section S7 for solid state characterization.

Overall, we demonstrated precise control over the templated nanoparticle size. Nanoparticle size follows a simple scaling relationship from the nanodroplet size, enabling the design of custom nanoparticles between 100 and 1000 nm. Since nanoemulsion droplet size is easily tuned,[48] our approach directly carries this tunability over to the resulting solid-state nanoparticles. In contrast, conventional top-down nanoparticle production through milling struggles to access nanoparticle sizes between 500 and 1000 nm, which is a size regime of particular interest for formulation design.[50] We demonstrated templating nanoparticles from three APIs (CBD, FEN, and VitD) in this size regime (Figure 3c). Other bottom-up methods struggle to control nanoparticles size with the level of precision and directness we report. For example, the emulsion freeze-drying approach developed by Grant and Zhang reported nonmonotonic dependence of nanoparticle size on the original emulsion droplet size.[51] In FNP, the organic solvent plays a critical role in the resulting nanoparticle size, with mechanisms governed by complex scaling relationships which are not easily tuned.[52,53] Particle size is considered a critical quality attribute for nanoformulations,[54] so size control is crucial to advance the quality-by-design (QbD) framework being adopted in drug product design.[55]

We also demonstrated that our templated API nanoparticles exhibit stability in their size distribution and solid state at room temperature and pressure for at least 6 months. This is a promising time scale for drug product supply chains, and represents a major advantage of our approach. Nanoparticles prepared from FNP usually exhibit suspension stability between 1 day up to 1 week,[56,57] and in some cases their shelf life has been engineered for up to 1 month.[57] Since nanoparticle suspension stability is difficult to engineer, researchers have turned to solidifying a preformed nanosuspension, using spray drying or lyophillization, for example.[58] However, processing nanosuspensions using these comparatively harsh processes can lead to aggregation.[59] Lyophillized nanoparticles also exhibit poor drug retention during storage.[60] In contrast, our comparatively gentle evaporative approach simultaneously forms nanoparticles and stabilizes them inside an excipient matrix, conferring a long shelf life. This supports another key application of our nanoparticle-loaded films; suspensions-on-demand. Our films are easily redispersible

https://doi.org/10.1021/acs.chemmater.5c02892
Chem. Mater. XXXX, XXX, XXX−XXX

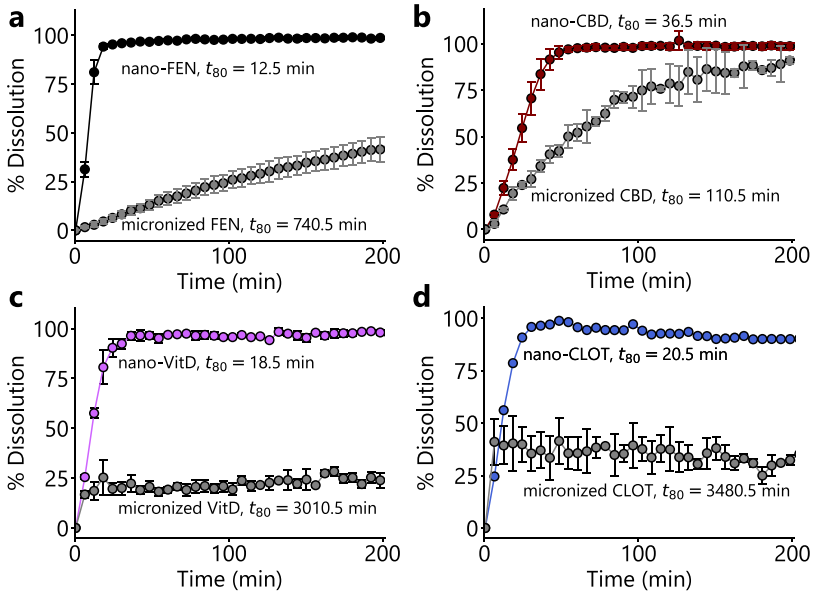

Figure 4. Nanosizing enhances API dissolution in biorelevant release media. Release testing was performed on the formulation with SOR 1:3 for each API: (a) FEN, (b) CBD, (c) VitD, and (d) CLOT. *Y*-axis shows % dissolution, while *X*-axis shows time in minutes. Colored points represent the nano-API thin films, while gray points represent the micronized API powders with solubilizing excipients. Points are averaged across three dissolution vessels, and error bars represent one standard deviation. The time to reach 80% dissolution (t_{80}) is shown for both the nano-API and micronized controls on each plot.

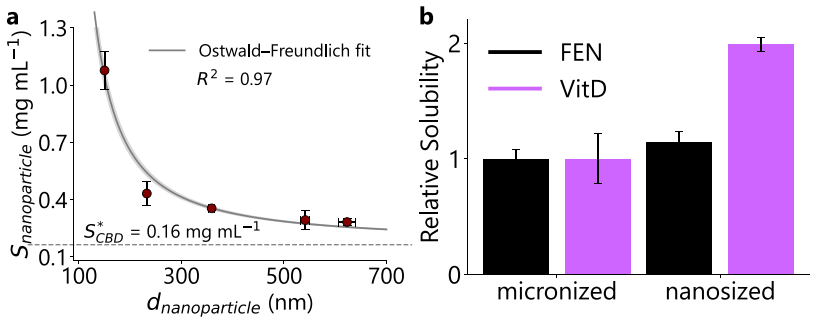

Figure 5. Nanosizing increases apparent thermodynamic solubility. (a) The intrinsic solubility of CBD nanoparticles ($S_{nanoparticle}$, mg mL^{-1}) as a function of the nanoparticle size ($d_{nanoparticle}$, nm). $S_{nanoparticle}$ was calculated using eq 5, accounting for the solubilizing effect of excipients in the thin film nanoformulations and the baseline micronized CBD solubility (S_{CBD}* = 0.16 mg mL^{-1}). The red circles represent the mean $S_{nanoparticle}$, averaged over 4 measurements (See Supporting Information Section S10), where the vertical error bar represents the standard deviation. The horizontal error bar represents the measurement standard deviation in $d_{nanoparticle}$ from DLS measurements. The gray curve indicates the fit for the Ostwald–Freundlich eq (eq 4), which achieves R^2 = 0.97 for N = 5 using nonlinear least-squares. The fitted interfacial tension between solid CBD and the dissolution media is γ = 0.52 ± 0.01 mN m^{-1}, where the uncertainty represents the standard error in the parameter estimation. This uncertainty is represented through the shaded area around the solid line. (b) Bar chart showing the relative solubility enhancement of nanosizing FEN and VitD particles. The micronized API with excipients are shown as the baseline relative solubility of 1, as measured through UV–vis absorbance. The solubility of the nanoformulations (formulated with SOR 1:3) is shown normalized against the micronized control. Black bars indicate relative solubility for FEN, while purple bars indicate relative solubility for VitD. See Supporting Information Section S10 for analytical details and calculations.

through either gentle vortex mixing or simple refrigeration (Figure 2e). They could thus serve as a long-term solid-state storage media for nanoparticles, ensuring robust stability without complex storage conditions and enabling simple point-of-care suspension preparation. These suspensions could be suitable for delivery via oral, intravenous, intramuscular, subcutaneous, or ocular administration.[4]

2.3. Nanoformulation Improves Bioavailability *In Vitro*

After establishing robust control over API nanoparticle size and stability, we demonstrate the impact of nanosizing on *in vitro* bioavailability. First, we highlight that the nanoparticle-loaded thin films exhibit rapid dissolution in biorelevant release media, in contrast to the slow dissolution of the micronized API (Figure 4). See Supporting Information Section S8 for sizing of the micronized API powders. For consistency, dissolution tests of micronized APIs include the same excipients as the nanoformulations (MC and surfactant) prepared as a "drugless" film with the same methodology as the nanoparticle-loaded films. This drugless excipient film and the micronized powders are then both added into the dissolution vessel, providing a kinetic advantage over the nanoformulation films which have to breakup before releasing API particulates. See Supporting Information Section S9 for dimensions of API-loaded films used for dissolution testing. The micronized API formulations exhibit slow dissolution,

https://doi.org/10.1021/acs.chemmater.5c02892
Chem. Mater. XXXX, XXX, XXX−XXX

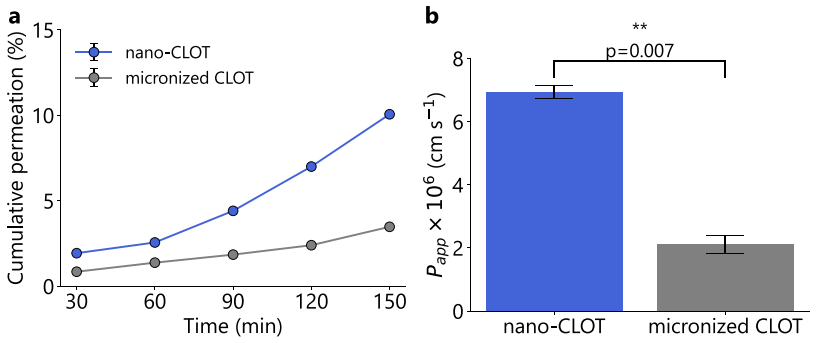

Figure 6. Nanosizing increases apparent permeability of CLOT. (a) Cumulative percentage of CLOT permeated across Caco-2 cell monolayer over 150 min. The blue points indicate average cumulative permeation for the nano-CLOT film formulated with SOR 1:3, while the gray points indicate average cumulative permeation for the micronized CLOT using the same excipient concentrations. The *y*-axis error bars represent the standard deviation between independent measurements (n = 2). The lines are included to guide the eye. (b) The average calculated apparent permeability coefficient (P_{app}, cm s^{-1}) for both the nano-CLOT (blue) and the micronized CLOT formulations (gray). *Y*-axis is multiplied by 1 × 10^6 for ease of visualization. Error bars represent standard deviation between independent calculations (n = 2). The P_{app} for the nano-CLOT and micronized CLOT were compared using a two-tailed unpaired t test, with significance (p = 0.007) indicated by asterisks above the bars (**p < 0.01).

with 80% of API dissolving (t_{80}) after 740.5 (FEN), 110.5 (CBD), 3010.5 (VitD), and 3480.5 (CLOT) min. The nanoparticle-loaded thin films exhibit rapid dissolutionm, with t_{80} of 12.5 (FEN), 36.5 (CBD), 18.5 (VitD), and 20.5 (CLOT) min (Figure 4a–d).

We next measured how the apparent thermodynamic aqueous solubility increases with decreasing nanoparticle size. This behavior is predicted by the Ostwald–Freundlich equation, as shown below

$$\ln\left(\frac{S_{\text{nanoparticle}}}{S^*}\right) = \frac{4M\gamma}{d_{\text{nanoparticle}}\rho RT} \tag{4}$$

where $S_{\text{nanoparticle}}$ is the instrinsic nanoparticle solubility (g mL^{-1}), S^* is solubility of a large particle (or the bulk solubility, g mL^{-1}), M is the molecular weight of the solute (g mol^{-1}), γ is the interfacial tension (mN m^{-1}) between a nanoparticle and the solvent, ρ is the density of the aqueous media (kg m^{-3}), R is the ideal gas constant, and T is temperature (K). This equilibrium description assumes particles are spherical and pure, the system is under constant external pressure, and that interfacial tension is isotropic and size-independent.[61] We quantitatively measured $S_{\text{nanoparticle}}$ in biorelevant aqueous media as a function of $d_{\text{nanoparticle}}$ for CBD. First, we established the solubility of the micronized CBD in the media by loading it in excess and allowing the sample to fully dissolve over 4 days, yielding S_{CBD}^* = 0.16 mg mL^{-1}. This was repeated for CBD-loaded films with varying $d_{\text{nanoparticle}}$ (Supporting Information Section S10). To isolate the effect of nanoparticle size and control for the solubilizing effect of the excipients in the thin film, we also prepared controls for each formulation with an excipient-only film and the micronized API. eq 5 details this calculation

$$S_{\text{nanoparticle}} = S_{\text{formulation}} - (S_{\text{control}} - S^*) \tag{5}$$

where $S_{\text{nanoparticle}}$ is the intrinsic nanoparticle solubility, $S_{\text{formulation}}$ is the total solubility for each nanoformulation (including the solubilization effect of excipients), and S_{control} is the solubility of the micronized CBD with the drugless excipient film at each formulation. The resulting $S_{\text{nanoparticle}}$ as a function of $d_{\text{nanoparticle}}$ is shown in Figure 5a. We observe apparent solubility increasing from 0.16 mg mL^{-1} for the micronized particles up to 1.08 mg mL^{-1} for 150 nm CBD nanoparticles. Including the solubilizing effect of the excipients, $S_{\text{formulation}}$ for the 150 nm CBD nanoparticles increases to 1.53 mg mL^{-1}, a 9.5 fold increase over S^* (Supporting Information Figure S15). Fitting the experimental $S_{\text{nanoparticle}}$ with eq 4 using nonlinear least-squares yields γ = 0.52 ± 0.01 mN m^{-1}. For FEN and VitD, the micronized powders dissolved too slowly to generate a reliable standard absorbance curve in the dissolution medium (Supporting Information Figure S16). We thus compared only the solubility enhancement of the nano-formulation (formulated with SOR 1:3) relative to the micronized control formulated with the same excipient concentrations. We observe that the nanosized FEN exhibits a ∼15% increase in solubility over the micronized control, while the nanosized VitD exhibits a ∼100% increase in solubility over the micronized control (Figure 5b).

Finally, we evaluated the effect of nanosizing on intestinal absorption, using a Caco-2 transwell permeability model, an established *in vitro* approach.[62] We first established cell viability of Caco-2 cell culture by performing a dose–response study with CLOT suspensions prepared from the SOR 1:3 formulation at 35, 167, 334, and 500 μM in Hank's balanced salt solution (HBSS). We found that cells tolerated up to 334 μM CLOT for 6 h (Supporting Information Section S11). We then evaluated the permeability of a nano-CLOT suspension and a micronized CLOT suspension (with the same excipient concentrations) across the Caco-2 monolayer. After 150 min, around 10% of the CLOT in the nanosuspension permeates across the Caco-2 monolayer, while only 3.5% of the CLOT in the micronized suspension permeates (Figure 6a). From the kinetic permeation data, we calculated an apparent permeability coefficient (P_{app}, see Experimental Section) for both formulations. The nano-CLOT formulation has P_{app} = 6.9 ± 0.2 × 10^{-6} cm s^{-1}, while the micronized formulation has P_{app} = 2.1 ± 0.3 × 10^{-6} cm s^{-1} (Figure 6b). Supporting Information Section S12 contains analytical details.

We observe that the nanoparticle-loaded thin films exhibit rapid dissolution kinetics (12.5 min < t_{80} < 36.5 min) in biorelevant release media compared to the micronized API formulations (1.84 h < t_{80} < 58.0 h). This enhancement in dissolution kinetics is critical to overcome dissolution-limited absorption for biopharmaceutical classification system (BCS)

https://doi.org/10.1021/acs.chemmater.5c02892
Chem. Mater. XXXX, XXX, XXX–XXX

class II APIs.[63] Rapid dissolution from thin films is crucial for delivering therapeutics for emergent conditions including allergies, motion sickness, seizure, hypertension and angina, where t_{80} < 20 min is essential for effective delivery.[34,64,65] While our objective was to demonstrate rapid dissolution of the API nanoformulations, the thin film form factor offers facile control over the dissolution time scale. Previous work focused only on FEN nanoparticle-loaded films found that film thickness set the dissolution timescale because solubilization is limited by film hydration and breakup rather than nanoparticle dissolution.[25]

Despite its widespread citation in the literature, there has been very limited published work validating the Ostwald−Freundlich equation. A few studies have attempted to correct the derivation or the thermodynamic interpretation. For example, Kaptay developed a corrected form of the Ostwald−Fruendlich equation and argued the increase in apparent solubility is not due to the increased curvature of the solid phase (as commonly claimed), but rather due to the increased specific surface area of the solid phase.[61] Similarly, Buckton and Beezer argued that the apparent solubility increase is ultimately a kinetic effect, and warned researchers against attributing the effect to thermodynamics.[66] Far fewer studies have actually validated the relationship experimentally. Van et al. rigorously developed and evaluated methods to determine the apparent solubility of loviride as a function of nanoparticle size, but observed only a 15% increase over the bulk solubility.[67] In contrast, Kim et al. found a 2× increase in the apparent solubility of 200 nm glycine nanoparticles, which is more typical of the large solubility increase the pharmaceutical literature has traditionally claimed from nanosizing.[68] In our case, the smallest CBD nanoparticles exhibited a ∼6.75× increase in apparent solubility over the bulk micronized CBD powder due to nanosizing. The larger solubility enhancement that we observe is likely because our CBD nanoparticles are amorphous and thus would have higher energy surfaces than the crystalline CBD micronized powder.[67] We can further validate the reasonableness of our results by comparing the fitted interfacial tension value (γ = 0.52 mN m^{-1}) to an estimate using an equation derived from Bragg−Williams regular solution theory,[69] which Van et al. also used to validate their measurements. This relationship is shown below in eq 6

$$\gamma = -\frac{0.33 k_B T}{\left(\frac{V_m}{N_A}\right)^{2/3}} \ln\left(\frac{S^*}{55.6} + 5\right) \quad (6)$$

where k_B is the Boltzmann constant, V_m is the molar volume of the solute, N_A is Avogadro's number, and S^* is the molar bulk solubility.[69] Using eq 6, the estimated γ is 0.33 mN m^{-1}, comparable to but slightly smaller than the fitted value. We expect this estimate to be smaller than the fitted γ value, since the S^* used in eq 6 describes the bulk solubility for crystalline particles, so the calculated γ value is likely underestimated given the amorphous nanoparticles exhibit higher energy surfaces. These interfacial tension values are slightly lower than the typical values for pharmaceutical compounds in water (5−50 mN m^{-1}), likely because these solubility experiments were performed in a biorelevant medium containing surfactant (see Experimental Section). Since solubility has direct implications for *in vivo* bioavailability, understanding the solubility enhancement from an enabling formulation is crucial toward optimizing formulation design.[70]

Nanosuspensions prepared from the thin films also exhibit enhanced permeation across Caco-2 monolayers. We observe a 3.3× enhancement in permeation between a micronized CLOT formulation and a CLOT nanoformulation. The micronized CLOT exhibited P_{app} = 2.1 ± 0.3 × 10^{-6} cm s^{-1}, which lies near the lower limit of the moderate permeability range defined for Caco-2 permeability ($10^{-6} < P_{app} < 10^{-5}$ cm s^{-1}).[62] In contrast, the nano-CLOT showed a P_{app} = 6.9 ± 0.2 × 10^{-6} cm s^{-1}, placing it near the upper end of this range. Given the strong correlation between the Caco-2 permeability of a formulation and its bioavailability for passively absorbed actives like CLOT,[71,72] this 3.3× enhancement represents a substantial increase in potential bioavailability. While the Caco-2 assay we performed does not reveal the mechanism of permeability enhancement, previous studies have identified the particle drifting effect as the likely mechanism for passive permeability enhancement of nanosized particles.[72,73] This theory proposes that nanoparticles reduce the effective diffusional resistance of the aqueous boundary layer near the membrane by locally supplying dissolved drug, suggesting that both faster nanoparticle diffusion and dissolution drive permeation enhancement. In future work, we could confirm whether the observed permeation enhancement follows the particle drifting effect by evaluating permeability as a function of nanoparticle size, analogous to the quantification we performed for solubility enhancement.

3. CONCLUSION

We demonstrated applying nanoemulsion templating to formulate size-controlled API nanoparticles inside a hydrogel thin film. By using different dispersed phase solvents, we formulate four chemically diverse APIs using this approach. The size of the templated API nanoparticles is controlled through the precursor droplet size, enabling customized nanoparticle sizes between 100 and 1000 nm. These nanoparticles are simultaneously formed and stabilized in the thin polymer film, conferring long-term stability (>6 months) when stored at room temperature and pressure, accessing stability time scales which are comparable to drug product supply chains. We highlight the *in vitro* bioavailability enhancement conferred by nanosizing through kinetic dissolution, apparent thermodynamic solubility, and cellular permeability enhancement. Our quantitative demonstration of solubility enhancement as a function of nanoparticle size, which is rare in the literature, can be accurately modeled using the Ostwald−Freundlich Equation. Our approach can be applied industrially as a rapid fit-for-purpose approach to generate enabling formulations. The thin film form factor explored in this study is relevant for emergent conditions, buccal delivery, and oral delivery to elderly, pediatric, and dysphagic patients. The long-term shelf storage we report also unlocks these thin-film nanoformulations for applications in 'suspensions-on-demand,' giving point-of-care access to shelf-stable suspensions. Overall, we demonstrate a general and tunable approach for versatile applications in pharmaceutical nanoformulation.

https://doi.org/10.1021/acs.chemmater.5c02892
Chem. Mater. XXXX, XXX, XXX−XXX

4. EXPERIMENTAL SECTION

4.1. Materials

Methylcellulose (viscosity: 15 cP, $M_w \approx 14{,}000$ g mol^{-1}), fenofibrate, anisole, Tween 80 (polysorbate 80), Span 80 (sorbitan monooleate), FEN, VitD, CLOT, anisole, *n*-butanol, ethyl acetate, sodium dodecyl sulfate (SDS), fibronectin, and phosphate buffer saline (PBS) were purchased from Sigma-Aldrich and used without further modification. CBD isolate was purchased from Vantage Hemp and used without further modification.

4.2. Saturated API Organic Solutions

The saturated solutions of APIs in organic solvents were prepared according to the saturation concentrations determined. FEN was dissolved in anisole at 0.45 mass fraction. CBD was dissolved in anisole at 0.62 mass fraction. CLOT was dissolved in *n*-butanol at 0.095 mass fraction. VitD was dissolved in ethyl acetate at 0.58 mass fraction. Each solution was prepared by first adding the solvent to a vial, then adding the API powder at the appropriate mass fraction. The mixtures were then stirred at 700 rpm and 45 °C to accelerate dissolution. After the API was dissolved, the solution was taken off the heating and stored at room temperature. Supporting Information Section S2 contains information about the measurement of these saturation concentrations.

4.3. Nanoemulsion Synthesis

The API-loaded nanoemulsions were prepared with thermogelling capability consist of a continuous aqueous phase (5 wt % MC aqueous solution) and a dispersed organic phase (saturated API-in-solvent). To synthesize the nanoemulsions, a pre-emulsion was prepared by first adding the optional surfactant (Tween80 or Span80), the continuous phase, and the dispersed phase into a 50 mL conical Falcon Tube, then vortexing the mixture for 30 s to generate a pre-emulsion. The nanoemulsion formulations for different surfactant to oil ratios (SORs) are summarized in Supporting Information Table S1. The masses of the continuous and dispersed phases were fixed at 3.0 and 0.03 g respectively, such that only surfactant mass was varied. The pre-emulsion mixture was then placed in a 24 mm diameter horn ultrasonicator (Cole-Parmer) and sonicated at 30% amplitude for 30 min at a frequency of 20 kHz. The ultrasonicator was kept at 10 °C with a circulating cooling water bath.

4.4. Preparation of Nanoparticle-Loaded Thin Films

A 75 mm × 25 mm × 1 mm microscope slide (plain glass, VWR VistaVision) was used as a substrate for the thin film. The mass of nanoemulsion on each slide was fixed at 2.0 g. After the nanoemulsion was transferred via pipet onto the slide, the slide was quickly moved to a VWR Symphony Vacuum Oven and dried for 24 h to evaporate the anisole and water. For FEN, CBD, and CLOT, the thin films were dried at 70 °C with no vacuum. For VitD, the thin films were dried at 50 °C, pulling vacuum at −50 mmHg, since VitD is temperature-labile. Once dried, the thin film was removed from the slide and stored in a closed vial at room temperature for further characterization and analysis.

4.5. Dynamic Light Scattering

Dynamic light scattering (DLS) was performed using a Brookhaven NanoBrook 90Plus PALS at a fixed scattering angle of 90° and temperature of 25 °C. The sample was prepared by diluting 5 μL of nanoemulsion in 3 mL of DI water in a cuvette. Five sets of 1 min measurements were performed for each sample to characterize the droplet size distribution.

4.6. Differential Scanning Calorimetry

Thermal analysis of the thin films were performed using a differential scanning calorimeter (TA Instruments DSC 2500). The sample chamber environment was kept inert using a nitrogen purge at a flow rate of 50 mL min^{-1}. Approximately 5 mg of ground sample was loaded into Tzero pans and lid. The sample was equilibrated at 10 °C, then the temperature was ramped up to 150 °C at a ramp rate of 10 °C min^{-1}. Then, an isothermal step at 150 °C was held for 5 min.

4.7. Scanning Electron Microscopy

The solid-state morphology of the dried thin films was characterized using a high-resolution scanning electron microscope (Zeiss HRSEM). Samples were prepared on SEM specimen stubs with carbon tape and sputter-coated with 5 nm of gold prior to imaging to improve contrast. An accelerating voltage of 3 kV and a probe current of 120 pA were used.

4.8. Transmission Electron Microscopy

API nanoparticles were characterized using an FEI Tecnai G2 Spirit TWIN TEM equipped with a LaB6 filament, operating at an accelerating voltage of 120 kV. To prepare a suspension of API nanoparticles, 10 mg of nanoformulated thin films were dissolved in 10 mL of water, which dissolved the MC thin film matrix and liberates the nanoparticles. This suspension was then drop-cast onto carbon film-supported copper grids (size 200 mesh), and bright-field microscopy images were taken using a Gatan CCD camera. The resulting images were analyzed using ImageJ. Supporting Information Section S6 contains additional representative TEM images.

4.9. X-ray Diffraction

The solid state structures of the drugs loaded in the thin films were characterized via X-ray diffraction (XRD) using an in-reflection mode (Phillips PANalytical X'Pert Pro MPD). The instrument was operated at a constant voltage of 45 kV and a constant current of 20 mA. For preparing the samples, the dried thin films were ground with a mortar and pestle into a fine powder suitable for XRD analysis. The powder sample was placed on a silicon crystal zero diffraction plate. The diffraction angle 2-θ was swept from 4° to 40° by 0.0167° at a scanning rate of 2° min^{-1}.

4.10. Drug Loading Analysis

The drug loading content of the nanoformulated thin films were analytically characterized using UV−vis spectroscopy (ThermoFisher Scientific NanoDrop One/OneC Spectrophotometer). First, 10 mg of thin film was suspended in 3 mL of EtOH in a 10 mL conical Falcon tube. The tube was vortexed, dissolving the API nanoparticles loaded in the film. Next, 100 μL of the sample was diluted 10× into fresh ethanol to ensure that the concentration was in the regime of linear absorbance response. The sample's UV absorbance was measured at the appropriate λ_{max} (287 nm for FEN, for instance), the concentration was determined via a linear interpolation into the respective calibration curve, and the drug loading by mass was calculated from the concentration. Supporting Information Section S4 details this analytical determination.

4.11. Sizing of Micronized API Particles

The PSD of the micronized API particles were characterized using a BlazeMetrics BlazePlatform equipped with a Meso probe in dark-field microscopy mode. An aqueous suspension of the micronized powders was prepared in a 20 mL vial. The probe was directly inserted into the suspension, which was continuously mixed with a magnetic stir bar on a mixing plate to ensure uniform dispersion. Once the PSD equilibrated, PSD statistics were obtained from real-time imaging using the BlazeMetrics software. The length-weighted PSDs are provided in Supporting Information Section S8, and the mean $d_{crystal}$ for each API were extracted from these PSDs.

4.12. Dissolution Testing

The *in vitro* kinetic dissolution of API from the thin film nanoformulations was measured using a USP Dissolution Apparatus II (Agilent Technologies Varian VK 7025). A Cary 50 UV−vis spectrometer and an *in situ* probe set were integrated into the dissolution test in order to automatically record the absorbance at the λ_{max} for each API every minute. For each API, an appropriate biorelevant release media was used based on prior work in the literature and FDA guidance for dissolution testing.[32] For FEN, 0.72 wt % sodium dodecyl sulfate (SDS) was used.[25,29] For CBD, 0.5 wt % SDS in 1× PBS was used.[36] For CLOT, 0.5 wt % SDS was used.[74] For VitD, 0.3 wt % SDS was used.[75] The vessel was operated at 37 °C and 75 rpm, and the drug concentration was set to 15 μg mL^{-1}. Since the

https://doi.org/10.1021/acs.chemmater.5c02892
Chem. Mater. XXXX, XXX, XXX−XXX

drug loading content in the film varies between each API, the film dimensions were adjusted to meet this concentration (Supporting Information Section S9). Each thin film was placed into a USP-compliant Japanese Pharmacopeia sinker basket to decrease the variability of the release results caused by the thin films floating.[76] The release experiment for each formulation was performed in triplicate.

4.13. Determination of Nanoparticle Solubility

The apparent thermodynamic solubility of API in dissolution media was measured to illustrate the effect of nanoparticle size on solubility. For CBD, first a standard curve of CBD in biorelevant dissolution media (0.5% SDS in 1× PBS) was established in the linear UV-concentration regime, far below saturation concentration (Supporting Information Figure S14a,b). Next, the solubility of the bulk micronized sample was measured without any excipients. To ensure complete saturation, 50 mg of API powder was added to 10 mL of media (5 g L^{-1}, >5000 X literature value of aqueous solubility). The mixture was stirred at 300 rpm on a stir plate. Aliquots were taken daily for four consecutive days and ultracentrifuged at 4000 rpm for 15 min to pellet out any undissolved CBD particles. The supernatant was serially diluted (1×, 5×, 10×, 50×, and 100×) and the UV absorbance was measured for each dilution to yield a robust concentration determination through interpolation in the standard curve. To control for the effect of the excipients in the thin film on dissolution enhancement, the above protocol was repeated with the addition of "drugless" thin films at the same ratio as the nanoformulated thin films. Supporting Information Figure S15 shows the measured concentration of the different nanoformulations and control formulations over the 4 days when measurements were taken. The concentrations measured on days 2−4 (after the concentration plateaus) were averaged to get $S_{formulation}$ and $S_{control}$, which were then used in eq 5 to calculate $S_{nanoparticle}$.

4.14. Caco-2 Cell Culture

Caco-2 was acquired (ATCC HTB-37) and cultured in T75 flasks (Corning 430641U) prior to viability or permeability studies. Media exchange was performed every other day using Eagle's minimum essential medium (EMEM, 30−2003), 20% FBS (Corning 35−016-CV) and 1% Pen-Strep (GenClone 25−512). Passages 19 and 20 were used in this study.

4.15. Cell Viability

A dose−response study was performed on 24 well-plate to determine the maximum viable CLOT concentration for the permeability assay. Each well was coated with a 1:10 dilution of PBS:Fibronectin (Sigma FC010−5MG), and cells were seeded at 25k per well. On day 3, two sets of wells were treated for 6 and 24 h with CLOT suspensions prepared from the SOR 1:3 formulation, at 50, 100, 167, and 500 μM CLOT. Wells were then washed with PBS and incubated with ReadyProbes Cell Viability Imaging Kit (ThermoFisher R37609) for 30 min, where dead cells are stained green and all cells are stained blue. Cells were imaged using a EVOS M5000 Imaging System, and viability was calculated using eq 7 below

$$\text{viability } \% = \left(1 - \frac{N_{dead}}{N_{total}}\right)\cdot 100 \tag{7}$$

where N_{dead} indicates the number of dead cells, and N_{total} indicates the total number of cells counted. The cell viability results are summarized in Supporting Information Section S11.

4.16. Transwell Cell Culture

Transwell plates (Sigma CLS3413−48EA) were preincubated (37 °C, 5% CO2) for 30 min with 150 and 750 μL media in the apical and basal side, respectively. Cells from confluent culturing flasks were counted using Countess 3 Automated Cell Counter and reconstituted as a 300k mL^{-1} cellular suspension. Before plating the cells, the media were removed from the plates, and the basal side was refreshed with 750 μL. Next, ∼40k cells were seeded onto each apical side (150 μL of the diluted cell suspension). Plates were cultured in the incubator for 27 days. Media in both basal and apical sides were exchanged every other day until day 8. After day 8, media in the apical side were exchanged every day, while the basal side continued with media exchanging every other day. On day 27, the apical and basal sides were washed twice (200 μL apical, 600 μL basal) with PBS. Both apical and basal sides were then washed twice with warmed HBSS (Thermofisher 14025092). Plates were then incubated for 30 min in HBSS in preparation for the permeability assay.

4.17. Permeability Assay

After culturing cells in the transwells, the permeability assay was performed on the Caco-2 monolayers. Nano-CLOT (formulated with SOR 1:3) and micronized CLOT (formulated with the same excipient concentrations) were prepared in HBSS at a concentration of 167 μM. These suspensions were warmed to 37 °C. The plates (6 wells per treatment group) were replaced with fresh 600 μL HBSS in the basal side, while the apical side were replaced with 200 μL of the 150 μM CLOT suspensions. 200 μL samples from the basal side were collected every 30 min for 150 min and replaced with 200 μL HBSS each time. At the final time point (150 min), all 600 μL were collected from the basal side and all 200 μL were collected from the apical side. Samples were stored in −20 °C until HPLC analysis. Using a Millicell ERS-2 Voltohmmeter (Millipore MERS00002), TEER measurement was taken before and after treatment with the CLOT suspensions to ensure the suspensions did not degrade the barrier integrity beyond usability. The change in measured TEER measurements is provided in Supporting Information Figure S20.

4.18. HPLC Analysis and Apparent Permeability Coefficient Determination

After performing the permeability assay, the mass of CLOT permeated at each time point was analytically determined via HPLC UV−vis, using an Agilent Model 1100, with a C18 reverse phase column (Vydac 218TP52, 2.1 mm × 250 mm). To ensure the permeated CLOT in the basal side was detectable via HPLC UV−vis, the 200 μL aliquots collected from 3 wells per treatment group were combined into a single sample for analysis. Since six wells were treated per group, this yielded two independent replicates for each time point and treatment condition. Each combined sample (600 μL) was diluted to a final volume of 1.4 mL prior to injection. A 1.2 mL aliquot was injected at a flow rate of 0.3 mL min^{-1}. The elution gradient used was 5−5%B (0−5 min) to 100%B (5−65 min), where A is 0.05% trifluoroacetic acid (TFA) and B is 0.043% TFA and 80% acetonitrile. CLOT eluted at 37 min and was detected at λ_{max} = 210 nm. A calibration curve relating chromatographic peak area to CLOT concentration was established using standard solutions of CLOT (Supporting Information Section S12). Sample concentrations were determined by interpolation from this calibration curve. The apparent permeability coefficient for the apical to basal transport P_{app} was calculated from the permeation data using eq 8 below

$$P_{app} = \frac{\frac{dQ}{dt}}{C_0 A} \tag{8}$$

where $\frac{dQ}{dt}$ is the permeation rate, C_0 is the initial concentration of CLOT in the donor (apical) compartment, and A is the area of the transwell on which the cell monolayer is cultured.

■ ASSOCIATED CONTENT

Supporting Information

The Supporting Information is available free of charge at https://pubs.acs.org/doi/10.1021/acs.chemmater.5c02892.

Nanoemulsion formulations, Determination of API solubility in organic solvents, SEM microscopy and film pliability, Determination of drug loading, Full DLS measurements of nanodroplet and nanoparticle size distributions, TEM images of API nanoparticles, API nanoparticle solid state stability, Sizing of micronized drug powders, Dimensions of thin films used in

https://doi.org/10.1021/acs.chemmater.5c02892
Chem. Mater. XXXX, XXX, XXX−XXX

dissolution testing, Nanoparticle solubility determination, Cell viability, HPLC chromatograms and percent TEER change, Residual Solvent Estimation (PDF)

AUTHOR INFORMATION

Corresponding Author

Patrick S. Doyle − *Department of Chemical Engineering, Massachusetts Institute of Technology, Cambridge, Massachusetts 02139, United States;* orcid.org/0000-0003-2147-9172; Email: pdoyle@mit.edu

Authors

Lucas Attia − *Department of Chemical Engineering, Massachusetts Institute of Technology, Cambridge, Massachusetts 02139, United States;* orcid.org/0000-0002-9941-3846

‡**Dien Nguyen** − *Department of Chemical Engineering, Massachusetts Institute of Technology, Cambridge, Massachusetts 02139, United States;* orcid.org/0009-0000-9229-4154

Kevin Liu − *Department of Chemical Engineering, Massachusetts Institute of Technology, Cambridge, Massachusetts 02139, United States;* orcid.org/0009-0000-5633-1472

Qin M. Qi − *Department of Chemical Engineering, Massachusetts Institute of Technology, Cambridge, Massachusetts 02139, United States;* orcid.org/0000-0003-4925-4880

Complete contact information is available at: https://pubs.acs.org/10.1021/acs.chemmater.5c02892

Author Contributions

†L.A. and D.N. contributed equally to this work.

Notes

This report was prepared as an account of work sponsored by an agency of the United States Government. Neither the United States Government nor any agency thereof, nor any of their employees, makes any warranty, express or implied, or assumes any legal liability or responsibility for the accuracy, completeness, or usefulness of any information, apparatus, product, or process disclosed, or represents that its use would not infringe privately owned rights. Reference herein to any specific commercial product, process, or service by trade name, trademark, manufacturer, or otherwise does not necessarily constitute or imply its endorsement, recommendation, or favoring by the United States Government or any agency thereof. The views and opinions of authors expressed herein do not necessarily state or reflect those of the United States Government or any agency thereof.

The authors declare no competing financial interest.

‡D.N. Deceased on October 21, 2024.

ACKNOWLEDGMENTS

This work is dedicated to the memory of co-lead author Dien Nguyen, who was a brilliant scientist and wonderful person. This work was carried out in part through the use of MIT.nano's facilities. This work benefitted from facilities and equipment made available by the Institute for Soldier Nanotechnologies, a U.S. Army-sponsored UARC at MIT. This material is based upon work supported by the U.S. Department of Energy, Office of Science, Office of Advanced Scientific Computing Research, Department of Energy Computational Science Graduate Fellowship under Award Number DE-SC0022158. The authors acknowledge the MIT Undergraduate Research Opportunities Program for funding. This work was supported by the Koch Institute Frontier Research Program through the Kathy and Curt Marble Cancer Research Fund. The authors acknowledge the Koch Institute's Robert A. Swanson (1969) Biotechnology Center for technical support, specifically Heather Amoroso and Riley Abrashoff from the Biopolymers & Proteomics Core Facility. The table of contents figure was created in BioRender (access link: https://BioRender.com/ofpo0mvhttps://BioRender.com/ofpo0mv). Figure 1a was created in BioRender (access link: https://BioRender.com/95uterphttps://BioRender.com/95uterp).

REFERENCES

(1) Sun, D.; Gao, W.; Hu, H.; Zhou, S. Why 90% of clinical drug development fails and how to improve it? *Acta Pharm. Sin. B* **2022**, *12*, 3049−3062.

(2) Waring, M. J.; Arrowsmith, J.; Leach, A. R.; Leeson, P. D.; Mandrell, S.; Owen, R. M.; Pairaudeau, G.; Pennie, W. D.; Pickett, S. D.; Wang, J.; et al. An analysis of the attrition of drug candidates from four major pharmaceutical companies. *Nat. Rev. Drug Discovery* **2015**, *14*, 475−486.

(3) Kennedy, T. Managing the drug discovery/development interface. *Drug Discovery Today* **1997**, *2*, 436−444.

(4) Rabinow, B. E. Nanosuspensions in drug delivery. *Nat. Rev. Drug Discovery* **2004**, *3*, 785−796.

(5) Kawabata, Y.; Wada, K.; Nakatani, M.; Yamada, S.; Onoue, S. Formulation design for poorly water-soluble drugs based on biopharmaceutics classification system: basic approaches and practical applications. *Int. J. Pharm.* **2011**, *420*, 1−10.

(6) Agarwal, P.; Huckle, J.; Newman, J.; Reid, D. L. Trends in small molecule drug properties: A developability molecule assessment perspective. *Drug Discovery Today* **2022**, *27*, No. 103366.

(7) Li, K.; Crews, C. M. PROTACs: past, present and future. *Chem. Soc. Rev.* **2022**, *51*, 5214−5236.

(8) Liversidge, G. G.; Cundy, K. C. Particle size reduction for improvement of oral bioavailability of hydrophobic drugs: I. Absolute oral bioavailability of nanocrystalline danazol in beagle dogs. *Int. J. Pharm.* **1995**, *125*, 91−97.

(9) Loh, Z. H.; Samanta, A. K.; Heng, P. W. S. Overview of milling techniques for improving the solubility of poorly water-soluble drugs. *Asian J. Pharm. Sci.* **2015**, *10*, 255−274.

(10) Junyaprasert, V. B.; Morakul, B. Nanocrystals for enhancement of oral bioavailability of poorly water-soluble drugs. *Asian J. Pharm. Sci.* **2015**, *10*, 13−23.

(11) de Waard, H.; Frijlink, H. W.; Hinrichs, W. L. Bottom-up preparation techniques for nanocrystals of lipophilic drugs. *Pharm. Res.* **2011**, *28*, 1220−1223.

(12) Chan, H.-K.; Kwok, P. C. L. Production methods for nanodrug particles using the bottom-up approach. *Adv. Drug Delivery Rev.* **2011**, *63*, 406−416.

(13) Ristroph, K. D.; Pinkerton, N. M.; Markwalter, C. E.; D'Addio, S. M.; Gindy, M. E.; Pagels, R. F. 20 years of flash nanoprecipitation-from controlled precipitation to global medicine. *Adv. Drug Delivery Rev.* **2025**, *227*, No. 115700.

(14) Saad, W. S.; Prud'homme, R. K. Principles of nanoparticle formation by flash nanoprecipitation. *Nano Today* **2016**, *11*, 212−227.

(15) Sarkari, M.; Brown, J.; Chen, X.; Swinnea, S.; Williams, R. O., III; Johnston, K. P. Enhanced drug dissolution using evaporative precipitation into aqueous solution. *Int. J. Pharm.* **2002**, *243*, 17−31.

(16) Misra, S. K.; Pathak, K. Supercritical fluid technology for solubilization of poorly water soluble drugs via micro-and naonosized particle generation. *ADMET DMPK* **2018**, *8*, 355−374.

(17) Franco, P.; De Marco, I. Supercritical antisolvent process for pharmaceutical applications: A review. *Processes* **2020**, *8*, No. 938.
(18) Zhang, H.; Wang, D.; Butler, R.; Campbell, N. L.; Long, J.; Tan, B.; Duncalf, D. J.; Foster, A. J.; Hopkinson, A.; Taylor, D.; et al. Formation and enhanced biocidal activity of water-dispersable organic nanoparticles. *Nat. Nanotechnol.* **2008**, *3*, 506−511.
(19) Schenck, L.; Erdemir, D.; Gorka, L. S.; Merritt, J. M.; Marziano, I.; Ho, R.; Lee, M.; Bullard, J.; Boukerche, M.; Ferguson, S.; et al. Recent advances in co-processed APIs and proposals for enabling commercialization of these transformative technologies. *Mol. Pharmaceutics* **2020**, *17*, 2232−2244.
(20) Bosselmann, S.; Nagao, M.; Chow, K. T.; Williams, R. O. Influence of formulation and processing variables on properties of itraconazole nanoparticles made by advanced evaporative precipitation into aqueous solution. *AAPS PharmSciTech* **2012**, *13*, 949−960.
(21) Kalani, M.; Yunus, R. Application of supercritical antisolvent method in drug encapsulation: a review. *Int. J. Nanomed.* **2011**, 1429−1442.
(22) Pagels, R. F.; Edelstein, J.; Tang, C.; Prud'homme, R. K. Controlling and predicting nanoparticle formation by block copolymer directed rapid precipitations. *Nano Lett.* **2018**, *18*, 1139−1144.
(23) Fu, Z.; Li, L.; Wang, M.; Guo, X. Size control of drug nanoparticles stabilized by mPEG-b-PCL during flash nanoprecipitation. *Colloid Polym. Sci.* **2018**, *296*, 935−940.
(24) Zhu, Z. Flash nanoprecipitation: prediction and enhancement of particle stability via drug structure. *Mol. Pharmaceutics* **2014**, *11*, 776−786.
(25) Chen, L.-H.; Doyle, P. S. Design and use of a thermogelling methylcellulose nanoemulsion to formulate nanocrystalline oral dosage forms. *Adv. Mater.* **2021**, *33*, No. 2008618.
(26) Eral, H. B.; Lopez-Mejías, V.; O'Mahony, M.; Trout, B. L.; Myerson, A. S.; Doyle, P. S. Biocompatible alginate microgel particles as heteronucleants and encapsulating vehicles for hydrophilic and hydrophobic drugs. *Cryst. Growth Des.* **2014**, *14*, 2073−2082.
(27) Eral, H. B.; O'Mahony, M.; Shaw, R.; Trout, B. L.; Myerson, A. S.; Doyle, P. S. Composite hydrogels laden with crystalline active pharmaceutical ingredients of controlled size and loading. *Chem. Mater.* **2014**, *26*, 6213−6220.
(28) Domenech, T.; Doyle, P. S. High loading capacity nanoencapsulation and release of hydrophobic drug nanocrystals from microgel particles. *Chem. Mater.* **2020**, *32*, 498−509.
(29) Attia, L.; Chen, L.-H.; Doyle, P. S. Orthogonal Gelations to Synthesize Core−Shell Hydrogels Loaded with Nanoemulsion-Templated Drug Nanoparticles for Versatile Oral Drug Delivery. *Adv. Healthcare Mater.* **2023**, *12*, No. 2301667.
(30) Badruddoza, A. Z. M.; Godfrin, P. D.; Myerson, A. S.; Trout, B. L.; Doyle, P. S. Core-shell composite hydrogels for controlled nanocrystal formation and release of hydrophobic active pharmaceutical ingredients. *Adv. Healthcare Mater.* **2016**, *5*, 1960−1968.
(31) Chen, L.-H.; Doyle, P. S. Thermogelling hydroxypropyl methylcellulose nanoemulsions as templates to formulate poorly water-soluble drugs into oral thin films containing drug nanoparticles. *Chem. Mater.* **2022**, *34*, 5194−5205.
(32) FDA SCOGS (Select Committee on GRAS Substances). Title of the publication associated with this data set: GRAS Substances (SCOGS) Database
(33) Gupta, M. S.; Kumar, T. P.; Gowda, D. V. Orodispersible Thin Film: A new patient-centered innovation. *J. Drug Delivery Sci. Technol.* **2020**, *59*, No. 101843.
(34) Karki, S.; Kim, H.; Na, S.-J.; Shin, D.; Jo, K.; Lee, J. Thin films as an emerging platform for drug delivery. *Asian J. Pharm. Sci.* **2016**, *11*, 559−574.
(35) Kumar, R. Solubility and bioavailability of fenofibrate nanoformulations. *ChemistrySelect* **2020**, *5*, 1478−1490.
(36) Koch, N.; Jennotte, O.; Gasparrini, Y.; Vandenbroucke, F.; Lechanteur, A.; Evrard, B. Cannabidiol aqueous solubility enhancement: Comparison of three amorphous formulations strategies using different type of polymers. *Int. J. Pharm.* **2020**, *589*, No. 119812.
(37) Almarri, F.; Haq, N.; Alanazi, F. K.; Mohsin, K.; Alsarra, I. A.; Aleanizy, F. S.; Shakeel, F. Solubility and thermodynamic function of vitamin D3 in different mono solvents. *J. Mol. Liq.* **2017**, *229*, 477−481.
(38) Saadatfar, F.; Shayanfar, A.; Rahimpour, E.; Barzegar-Jalali, M.; Martinez, F.; Bolourtchian, M.; Jouyban, A. Measurement and correlation of clotrimazole solubility in ethanol+ water mixtures at T = (293.2 to 313.2) K. *J. Mol. Liq.* **2018**, *256*, 527−532.
(39) The United States Pharmacopeial Convention Residual Solvents. The United States Pharmacopeial Convention, 2019
(40) El Amri, N.; McKinstry, A.; Pollard, R. E.; Lewis, P. K.; Pinkerton, N. M. A Comparative Study of Flash Nanoprecipitation and Sequential Nanoprecipitation: Impact of Formulation Parameters on Drug-Loaded Nanoparticle Formation. *Mol. Pharmaceutics* **2025**, *22*, 6108−6119, DOI: 10.1021/acs.molpharmaceut.5c00835.
(41) Lewis, P. K.; El Amri, N.; Burnham, E. E.; Arrus, N.; Pinkerton, N. M. Process and Formulation Parameters Governing Polymeric Microparticle Formation via Sequential NanoPrecipitation (SNaP). *ACS Eng. Au* **2025**, *5*, 468−477.
(42) Attia, L.; Burns, J. W.; Doyle, P. S.; Green, W. H. Data-driven organic solubility prediction at the limit of aleatoric uncertainty. *Nat. Commun.* **2025**, *16*, No. 7497.
(43) Janßen, E. M.; Schliephacke, R.; Breitenbach, A.; Breitkreutz, J. Drug-printing by flexographic printing technology−A new manufacturing process for orodispersible films. *Int. J. Pharm.* **2013**, *441*, 818−825.
(44) Chen, Z.; Fu, Z.; Li, L.; Ma, E.; Guo, X. A cost-effective nano-sized curcumin delivery system with high drug loading capacity prepared via flash nanoprecipitation. *Nanomaterials* **2021**, *11*, No. 734.
(45) Caggiano, N. J.; Nayagam, S. K.; Wang, L. Z.; Wilson, B. K.; Lewis, P.; Jahangir, S.; Priestley, R. D.; Prud'homme, R. K.; Ristroph, K. D. Sequential Flash NanoPrecipitation for the scalable formulation of stable core-shell nanoparticles with core loadings up to 90%. *Int. J. Pharm.* **2023**, *640*, No. 122985.
(46) Wang, X.; Deng, F.; Ji, T.; Zhang, C.; Tian, Y.; Zhang, H.; Zheng, A.; Chen, Y.; He, B.; Dai, W.; et al. Impact of Physiological Characteristics on Chylomicron Pathway-Mediated Absorption of Nanocrystals in the Pediatric Population. *ACS Nano* **2024**, *18*, 23136−23153.
(47) Hoshyar, N.; Gray, S.; Han, H.; Bao, G. The effect of nanoparticle size on in vivo pharmacokinetics and cellular interaction. *Nanomedicine* **2016**, *11*, 673−692.
(48) Gupta, A.; Eral, H. B.; Hatton, T. A.; Doyle, P. S. Controlling and predicting droplet size of nanoemulsions: scaling relations with experimental validation. *Soft Matter* **2016**, *12*, 1452−1458.
(49) Attia, L.; Nguyen, D.; Gokhale, D.; Zheng, T.; Doyle, P. S. Surfactant-Polymer Complexation and Competition on Drug Nanocrystal Surfaces Control Crystallinity. *ACS Appl. Mater. Interfaces* **2024**, *16*, 34409−34418.
(50) Carling, C.-J.; Brülls, M. Milling of poorly soluble crystalline drug compounds to generate appropriate particle sizes for inhaled sustained drug delivery. *Int. J. Pharm.* **2021**, *593*, No. 120116.
(51) Grant, N.; Zhang, H. Poorly water-soluble drug nanoparticles via an emulsion-freeze-drying approach. *J. Colloid Interface Sci.* **2011**, *356*, 573−578.
(52) Vangeyte, P.; Gautier, S.; Jérôme, R. About the methods of preparation of poly (ethylene oxide)-b-poly (ε-caprolactone) nanoparticles in water: Analysis by dynamic light scattering. *Colloids Surf., A* **2004**, *242*, 203−211.
(53) Bovone, G.; Cousin, L.; Steiner, F.; Tibbitt, M. W. Solvent controls nanoparticle size during nanoprecipitation by limiting block copolymer assembly. *Macromolecules* **2022**, *55*, 8040−8048.
(54) Raines, K.; Agarwal, P.; Augustijns, P.; Alayoubi, A.; Attia, L.; Bauer-Brandl, A.; Brandl, M.; Chatterjee, P.; Chen, H.; Yu, Y. C.; et al. Drug dissolution in oral drug absorption: workshop report. *AAPS J.* **2023**, *25*, No. 103.

https://doi.org/10.1021/acs.chemmater.5c02892
Chem. Mater. XXXX, XXX, XXX−XXX

(55) Yu, L. X.; Amidon, G.; Khan, M. A.; Hoag, S. W.; Polli, J.; Raju, G.; Woodcock, J. Understanding pharmaceutical quality by design. *AAPS J.* **2014**, *16*, 771−783.
(56) Pustulka, K. M.; Wohl, A. R.; Lee, H. S.; Michel, A. R.; Han, J.; Hoye, T. R.; McCormick, A. V.; Panyam, J.; Macosko, C. W. Flash nanoprecipitation: particle structure and stability. *Mol. Pharmaceutics* **2013**, *10*, 4367−4377.
(57) Tao, J.; Chow, S. F.; Zheng, Y. Application of flash nanoprecipitation to fabricate poorly water-soluble drug nanoparticles. *Acta Pharm. Sin. B* **2019**, *9*, 4−18.
(58) Li, J.; Wang, Z.; Zhang, H.; Gao, J.; Zheng, A. Progress in the development of stabilization strategies for nanocrystal preparations. *Drug Delivery* **2021**, *28*, 19−36.
(59) Zuo, B.; Sun, Y.; Li, H.; Liu, X.; Zhai, Y.; Sun, J.; He, Z. Preparation and in vitro/in vivo evaluation of fenofibrate nanocrystals. *Int. J. Pharm.* **2013**, *455*, 267−275.
(60) Fonte, P.; Reis, S.; Sarmento, B. Facts and evidences on the lyophilization of polymeric nanoparticles for drug delivery. *J. Controlled Release* **2016**, *225*, 75−86.
(61) Kaptay, G. On the size and shape dependence of the solubility of nano-particles in solutions. *Int. J. Pharm.* **2012**, *430*, 253−257.
(62) Hubatsch, I.; Ragnarsson, E. G.; Artursson, P. Determination of drug permeability and prediction of drug absorption in Caco-2 monolayers. *Nat. Protoc.* **2007**, *2*, 2111−2119.
(63) Jünemann, D.; Dressman, J. Analytical methods for dissolution testing of nanosized drugs. *J. Pharm. Pharmacol.* **2012**, *64*, 931−943.
(64) Yardy, A.; Entz, K.; Bennett, D.; Macphail, B.; Adronov, A. Incorporation of loratadine-cyclodextrin complexes in oral thin films for rapid drug delivery. *J. Pharm. Sci.* **2024**, *113*, 1220−1227.
(65) Kanugo, A. Design Optimization and Evaluation of Patented Fast-Dissolving Oral Thin Film of Ambrisentan for the Treatment of Hypertension. *Recent Pat. Nanotechnol.* **2025**, *19*, 296−309.
(66) Buckton, G.; Beezer, A. E. The relationship between particle size and solubility. *Int. J. Pharm.* **1992**, *82*, R7−R10.
(67) Van Eerdenbrugh, B.; Vermant, J.; Martens, J. A.; Froyen, L.; Humbeeck, J. V.; Van den Mooter, G.; Augustijns, P. Solubility increases associated with crystalline drug nanoparticles: methodologies and significance. *Mol. Pharmaceutics* **2010**, *7*, 1858−1870.
(68) Kim, K.; Lee, I. S.; Centrone, A.; Hatton, T. A.; Myerson, A. S. Formation of nanosized organic molecular crystals on engineered surfaces. *J. Am. Chem. Soc.* **2009**, *131*, 18212−18213.
(69) Lindfors, L.; Forssen, S.; Westergren, J.; Olsson, U. Nucleation and crystal growth in supersaturated solutions of a model drug. *J. Colloid Interface Sci.* **2008**, *325*, 404−413.
(70) Murdande, S. B.; Pikal, M. J.; Shanker, R. M.; Bogner, R. H. Solubility advantage of amorphous pharmaceuticals: I. A thermodynamic analysis. *J. Pharm. Sci.* **2010**, *99*, 1254−1264.
(71) Pade, V.; Stavchansky, S. Link between drug absorption solubility and permeability measurements in Caco-2 cells. *J. Pharm. Sci.* **1998**, *87*, 1604−1607.
(72) Narula, A.; Sabra, R.; Li, N. Mechanisms and extent of enhanced passive permeation by colloidal drug particles. *Mol. Pharmaceutics* **2022**, *19*, 3085−3099.
(73) Adhikari, S.; Yang, D. H.; Li, N. Mass transport analysis of the particle drifting effect in a biphasic diffusion apparatus. *J. Pharm. Sci.* **2025**, *114*, No. 103937.
(74) Karolewicz, B.; Gajda, M.; Owczarek, A.; Pluta, J.; Górniak, A. Physicochemical characterization and dissolution studies of solid dispersions of clotrimazole with pluronic F127. *Trop. J. Pharm. Res.* **2014**, *13*, 1225−1232.
(75) Krishna, M. M.; Rao, S. V.; Venugopal, N.; Mantena, B. P. In vitro dissolution method for alendronate sodium and vitamin D3 tablets using HPLC with combination of refractive index and ultraviolet detectors. Analytical. *Chem. Lett.* **2015**, *5*, 216−228.
(76) Preis, M.; Woertz, C.; Schneider, K.; Kukawka, J.; Broscheit, J.; Roewer, N.; Breitkreutz, J. Design and evaluation of bilayered buccal film preparations for local administration of lidocaine hydrochloride. *Eur. J. Pharm. Biopharm.* **2014**, *86*, 552−561.

https://doi.org/10.1021/acs.chemmater.5c02892
Chem. Mater. XXXX, XXX, XXX−XXX